Electrochimica Acta 523 (2025) 145943

Contents lists available at ScienceDirect

Electrochimica Acta

journal homepage: www.journals.elsevier.com/electrochimica-acta

The influence of chromium oxide coating weight on filiform corrosion of trivalent chromium coatings for packaging steel

E. Bluett [a,*], J. Edy [b], M. Dodd [a], A.C.A. de Vooys [c], N. Wint [a], E. Jewell [a], H.N. McMurray [a]

[a] Faculty of Science and Engineering, Swansea University, Swansea UK
[b] Tata Steel, Research and Development, Swansea Technology Centre, Swansea, UK
[c] Tata Steel Research and Development, IJmuiden Technology Centre, The Netherlands

ARTICLE INFO

Keywords:
A. steel
A. metal coatings
C. oxide coatings
C. atmospheric corrosion
C. Polymer coatings

ABSTRACT

This paper describes a systematic study into the initiation and propagation of filiform corrosion (FFC) on industrially important Cr(III) coatings applied to packaging steel. FFC was initiated by introducing an artificial scribe into a model PVB organic coating which had been applied to the metallic coatings. The FFC corroded area was shown to decrease at increased values of Cr(III) oxide coating weight. This was explained largely due to the insulating properties of Cr(III) oxide. Chloride entrapment within the tail caused filament tapering. FFC was shown not to initiate on traditional electro chromium coated steel (ECCS).

1. Introduction

Hexavalent chromium (Cr(VI)) based electrolyte baths are traditionally used during the application of corrosion resistant coatings for packaging steel; the resultant product typically being referred to as either electro chromium coated steel (ECCS), or tin free steel (TFS). ECCS is typically produced as part of a continuous electrodeposition process. The coating is comprised of two distinct layers; a 50–140 mg.m^{-2} chromium underlayer and a 7–35 mg.m^{-2} native (hydr)oxide outer layer [1] which can either be applied via a one-step, or two-step process.

The low coating weights involved mean that the iron substrate may be exposed, particularly when the material undergoes substantial deformation, as is the case during the can forming process [2]. ECCS is therefore used in conjunction with an organic overcoat which provides additional corrosion protection. This polymer coated packaging steel product provides a high performance, economically viable and food-safe product [2]. However, the presence of an organic coating means that ECCS is susceptible to various modes of organic coating failure. Cathodic delamination is one such example of corrosion driven coating disbondment, which is a key failure process within the packaging industry. Anodic metal dissolution located in the defect is coupled with the cathodic delamination front by a thin electrolyte which ingresses underneath the coating [3].

Another form of organic coating failure is referred to as filiform corrosion (FFC). Unlike corrosion-driven cathodic delamination, where the separation of the organic overcoat from the metal substrate is linked to the cathodic reaction (usually oxygen reduction), in the case of FFC, separation of the coating from the substrate is generally linked to the anodic reaction [3,4]. Recent advancements in literature have demonstrated that the initial stage of FFC begins with anodic dissolution of exposed steel, and in the presence of group I cations, which are soluble at high pH, this then leads to cathodic delamination. This is due to the ability of group I cations to achieve electroneutrality with the OH^- generated at the cathode. In the subsequent phase, anodic undermining occurs at the delamination front, with chloride anions migrating to the leading edge [5]. It is generally believed that corrosion propagation involves two separate electrochemical sites, the anode and cathode, that differential aeration is the driving force for propagation and that contaminants effect the initiation stage. However, some key uncertainties remain regarding the exact location of the anodic and cathodic sites, the nature of the delamination front, the transport mechanisms for oxygen and water and whether an active outpost ahead of the propagating filament exists [5]. FFC occurs at high relative humidity (commonly 65 – 95 %) [6] and is known to occur on metals including aluminium and steel [7]. FFC occurs on packaging steel and it is commonly initiated by chloride electrolytes as well as organic acids such as acetic acid [8].

Fig. 1 shows a schematic of FFC processes, when initiated with a divalent metal chloride salt at a penetrative defect (scribe) in a polymer overcoat on iron. It is widely understood that propagation of the filament involves anodic dissolution at the leading edge of the 'active head'

* Corresponding author.
E-mail address: ellenbluett179@gmail.com (E. Bluett).

https://doi.org/10.1016/j.electacta.2025.145943
Received 16 December 2024; Received in revised form 21 February 2025; Accepted 26 February 2025
Available online 27 February 2025

of an individual filament [9]. Metal dissolution results in the undercutting of the organic coating and an acidic environment (approximately pH 4.5 in the head) is created due to the hydrolysis of aggressive anions, such as Cl^- [3,9,4,10]. In the case of iron, ferric hydroxide is left behind as the corrosion product in the 'inactive tail'. Oxygen is supplied to the cathode at the back of the filament head via diffusion through the porous tail of dry corrosion product or cracks in the coating, and allows FFC to propagate via a differential aeration process [11]. There is debate as to whether the entire filament tail in fact acts as the cathodic site opposed to only the back part of the FFC head [10]. The extent of these failure mechanisms should be considered when investigating new replacement products.

In recent years REACH legislation has imposed a restriction on the use of Cr(VI), which, in turn, has resulted in the drive by the steel packaging industry to find a suitable, non-toxic replacement [12,13]. This need is not unique to the packaging industry. Cr(VI) based coatings are used within a range of sectors, most notably aerospace. As such, trivalent chromium (Cr(III)) conversion coatings have been employed for the protection of aluminium alloys [14]. A recent study explored the use of a commercially available Cr(III) conversion coating to mitigate FFC on acrylic-coated steel using an electrochemical simulated approach. The experimental approach involved reproducing the anolyte and catholyte environments in the FFC interface and demonstrated that it was primarily the cathodic events that were inhibited by the coating [15]. Within the packaging industry, trivalent chromium-based chemistries have been used to develop alternatives to ECCS. Since first conception, the Cr(III) electroplating process has undergone iterative change, evolving from a one-step process, involving development of a single Cr-Cr oxide layer, to a two-step process which involves the application of a bilayer coating [16]. One such process, and the focus of this work, involves a steel strip being passed through a Cr(III) electrolyte bath where it is polarised in such a way that it becomes the cathode. For the first deposition step, a Cr(III) based electrolyte containing formate is used. This first step has been optimised to produce a Cr layer of ~100 $mg.m^{-2}$ thickness, comprising primarily of Cr metal. Chromium carbide (Cr_3C_2) is also present in the layer due to the use of formate in the electrolyte [17]. In the second deposition step, formate is not present in the Cr(III) based electrolyte, which enables a layer consisting primarily of Cr(III) oxide (Cr_2O_3) to be applied. For the purposes of this study, various plating parameters (line speed, anode passes, applied current) were varied to obtain coatings of varying amounts of Cr(III) oxide [17].

It is important to ensure that alternatives to ECCS are equivalent or better in terms of their performance. They should also be non-toxic, acceptable to the food industry, and ideally be capable of application under similar plating line conditions used for ECCS. As such, previous work [18] has compared the performance of Cr(III) coatings to ECCS, with respect to both cathodic delamination and FFC. Whilst there was no evidence of FFC on ECCS after 5 weeks, it was observed on the Cr(III) alternative, albeit at a lower propagation rate than that observed on uncoated steel. It was suggested that the chromium/chromium oxide based coating acted to retard the anodic reaction rate [18]. Later work demonstrated the ability of this Cr(III) alternative to resist corrosion-driven cathodic delamination once the Cr oxide coating weight had reached 20 $mg.m^{-2}$ (where the Cr layer remained at 122 $mg.m^{-2}$) [19]. It was proposed that elevated levels of Cr(III) oxide in the coating hindered interfacial electron transfer between the anode and cathodic delamination front.

However, the Cr(III) alternative used during these pieces of work was produced using a one-step electroplating process [20] whereby a mixed Cr metal – Cr oxide single layer was applied to the steel substrate. In comparison, very limited work has been conducted into the corrosion resistance properties of the bilayer Cr(III) alternative, when the Cr metal and Cr oxide are deposited in two separate stages, and no work has been published on its ability to withstand FFC.

As such, in this paper we present a systematic study into the initiation and propagation of FFC as it occurs on dual layer trivalent chromium based, Cr metal-Cr oxide coatings applied to packaging steels, as a function of Cr(III) oxide coating weight. The time dependant extent of FFC is investigated optically, and an explanation of the findings is given in terms of the effect of Cr(III) oxide coating weight. The results are also compared to ECCS, the current standard, as well as the aforementioned older style Cr(III) alternative; produced via a one-step electroplating process.

A combination of potentiodynamic polarisation (PDP), scanning electron microscope (SEM) and time of flight secondary ion mass spectroscopy (ToF-SIMS) is used to determine the differences in surface chemistry and appearance of the various oxide coating weights. This sample characterisation allowed hypotheses, with regards to the mechanism of FFC, to be formed. In this instance, PDP is used to characterise the anodic and cathodic currents observed for the different coating weights. ToF-SIMS is used to observe the elemental composition of the filaments after filiform had been initiated and propagated. SEM imaging allows for investigation of differences in the number of defects observed between samples of varying Cr(III) oxide coating weights.

2. Materials and methods

2.1. Materials

Developmental Cr(III) coated steel, produced on a Pilot Coating Line (PCL) at Tata Steel Packaging IJmuiden, were donated for this study. The as received samples had varying coating weights which were determined by XPS depth profiling. The process parameters and bath composition used to obtain these Cr(III) derived coatings is described

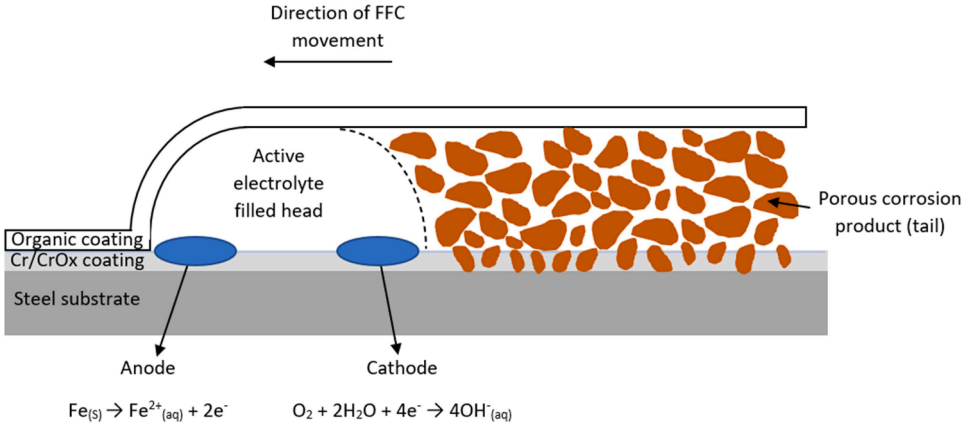

Fig. 1. Electrochemical processes that occur during filiform corrosion on steel.

elsewhere [21]. For the majority of the Cr(III) based substrates, electroplating had taken place via a two-step process to create a bilayer coating. The underlayer of Cr metal (100 mg.m^{-2}) was formed during the first electrodeposition step from a formate containing bath. The varying amounts of overlaying Cr(III) oxide were formed in a second electrodeposition step using a formate free bath. Various parameters, including the line speed, the number of anodes and the applied plating current were altered to control coating weight. Table 1 shows the different coating weights of the trivalent chromium coated samples made from the two-step electrodeposition process.

Unless otherwise stated, the coating weights values quoted are those listed in Table 1.

The previous iteration of the Cr(III) alternative, produced via a one-step cathodic electrodeposition process on an industrial electroplating line, were obtained from Tata Steel. Samples had comparable levels of Cr metal (~100 mg.m^{-2}), and Cr(III) oxide coating weights of 7 and 24 mg.m^{-2}.

Low carbon steel (blackplate), the substrate metal of the Cr(III) alternative, of 0.2 mm was sourced from Tata Steel, Trostre UK.

ECCS, produced on the pilot coating line using Cr(VI) electrolyte, had an as received Cr oxide coating weight of 9 mg.m^{-2} with the total thickness of both metal and oxide layers not exceeding 50 nm. All chemicals, including polyvinyl butyral-co-vinyl alcohol-co-vinyl acetate (PVB), molecular weight 70,000–100,000, were obtained from Sigma-Aldrich Chemical Co. and of analytical grade purity. A 15 % w/w ethanolic solution of PVB was made by slowly dissolving PVB in ethanol and used as the organic coating during experiments. Although PVB does not represent the fully formulated product, it dries at room temperature and allows for comparisons to be made easily between samples [18,22].

3. Methods

3.1. Filiform corrosion studies

Details of the methodology followed during FFC experiments have been described elsewhere [23]. In brief, 5 cm x 5 cm coupons were cut from a larger sheet of the Cr(III) alternative and degreased with isopropanol (IPA). Filiform was initiated at 3 artificial scribe defects per sample. Electrical tape, with a known thickness of 30 μm, was applied to two parallel edges of the sample and acted as a height guide during coating of PVB. A glass rod was used to bar-cast the samples with PVB, parallel to the rolling direction, resulting in an air-dried thickness of ~30 μm.

Once the PVB was dry, three 1 cm long artificial scribe defects were made in the PVB coatings, perpendicular to the rolling direction, using a scalpel. The direction of filiform propagation often aligns with the rolling direction [24], thus it was proposed that kinetic data would be more easily obtained if the filaments were predominantly travelling in a straight line. To compare results accurately between samples it was also important that the scribe direction was kept consistent. A syringe was used to introduce 2 μl of 0.005 M $FeCl_2$ electrolyte into the scribe, which has been shown to initiate FFC on iron elsewhere [25]. The experimental conditions were chosen to eliminate the possibility of cathodic disbondment occurring and to purely study FFC initiation and propagation kinetics.

Samples were then placed in a chamber where the temperature and relative humidity were kept constant at 20 °C and 75 % R.H. respectively. The humid atmosphere was maintained using a saturated NaCl solution and measured using a humidity sensor placed inside the chamber.

Table 1
The varying Cr(III) oxide coating weights overlaying the 100 mg.m^{-2} Cr metal.

Cr(III) oxide coating weights / mg.m^{-2}										
2.5	3	5.5	6.5	8	9	13	13.5	16.5	21.5	23.5

Samples were removed from the chamber at weekly time intervals over a period of 4 weeks to obtain photographs. Image analysis was carried out to calculate the FFC corroded area. The GIMP image analysis software was calibrated by specifying a pre-measured distance between two points and inputting the actual distance. The surface discoloration of the corroded parts of the samples enabled surface area measurements to be recorded. Six measurements were recorded for each different coating type.

3.1.1. Electrochemical measurements

Samples of size 2.5 × 2.5 cm were cut from a larger sheet and cleaned using isopropanol (IPA).

3.1.1.1. Open circuit potential (OCP). A 0.8 cm^2 area of the sample was exposed to 250 ml of 1 wt. % NaCl electrolyte, pH 2. OCP values were recorded at 20 °C, over a 2-hour time period, using a Gamry interface 1000. A 2-electrode set up was used consisting of the working electrode (substrate) and a saturated calomel reference electrode.

3.1.1.2. Potentiodynamic polarisation. A 0.8 cm^2 area of the sample was exposed to 250 ml of 0.6 mol.dm^{-3} NaCl electrolyte, pH 7. Potentiodynamic scans were conducted at 20 °C, using a Gamry interface 1000 and a scan rate of 0.1667 mV.sec^{-1}. A standard 3-electrode cell set up was used, consisting of the working electrode, saturated calomel reference electrode and a platinum counter electrode.

3.1.2. Microscopy

At the end of the 4-week FFC test period, a Zeiss axio observer Z1 M inverted optical microscope was used to determine the width and length of the filaments. Images of individual filaments were captured, and measuring tools on the microscope's software allowed distances across the width and length of the filaments to be measured accurately.

3.1.3. ToF-SIMS

Time of flight secondary ion mass spectrometry (ToF-SIMS) analysis was conducted using a Scientific Analysis Instruments (SAI) MiniSIMS-ToF. A gallium source was used to obtain secondary ion spectra to give elemental maps of the substrate surface. Chemical images and spectrums were obtained and analysed using MiniSIMS software. The software was able to convert the mass spectrometry data into an image so that each pixel represented an individual mass spectrum. Different elements were assigned colours to offer a visual representation of the surface chemistry on the substrate. To allow a better signal to noise ratio, and a greater number of counts, a dwell time of 5 ms per pixel was used [26]. Images were obtained with the detector in negative polarity to portray the negative ions emitted from the surface such that the presence of chloride could be identified [26].

3.1.4. X-ray photoelectron spectroscopy (XPS)

XPS spectra were recorded on a Kratos Axis Ultra using monochromated Al Kα X-rays of 1486.8 eV. The measured spot size was 700 μm x 300 μm. The XPS spectra was subsequently analysed in CasaXPS software with Shirley backgrounds. Binding energies were calibrated to the main hydrocarbon peak at 284.8 eV [1].

4. Results

4.1. Materials characterisation

Fig. 2 shows SEM images of the surface of the Cr(III) alternative substrates with a relative high (21.5 mg.m^{-2}) and low (2.5 mg.m^{-2}) Cr (III) oxide coating weight and were obtained prior to any other experimental procedures. These samples were chosen to quickly determine whether there were any changes in surface appearance of the coating as the coating weight was increased. The SEM images of the relative high

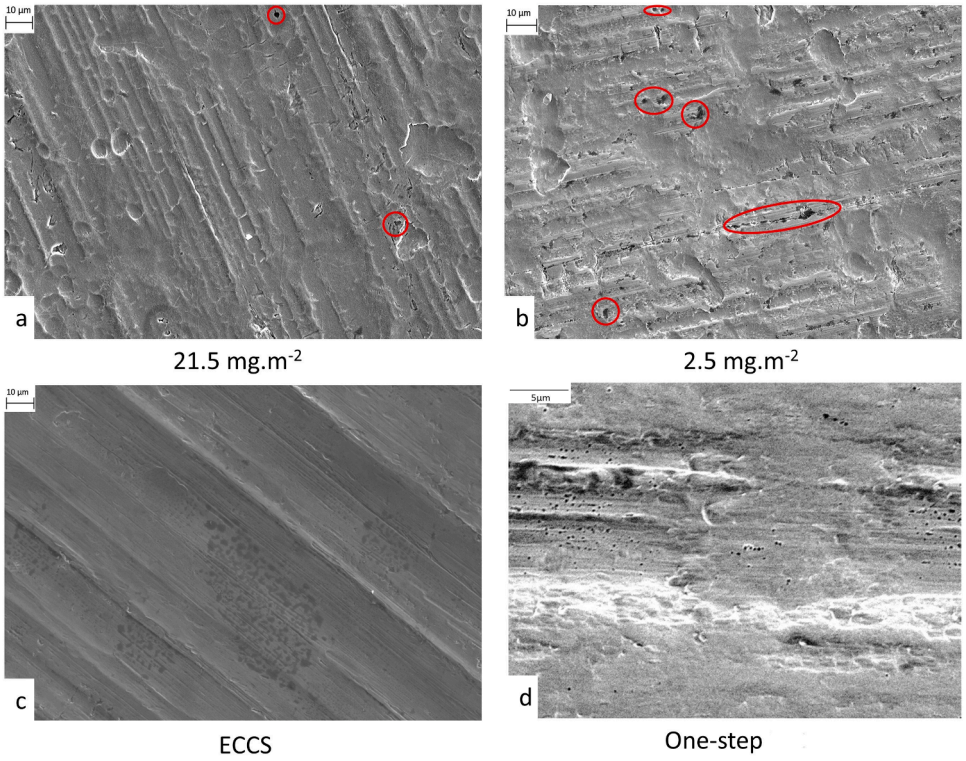

Fig. 2. SEM images of samples of the Cr(III) alternative with a Cr(III) oxide coating weight of 21.5 mg.m^{-2} (a) and 2.5 mg.m^{-2} (b), ECCS (c) and the Cr(III) alternative produced via the one step method (d) prior to experimental procedures. The presence of micropores on the relative high and low Cr(III) oxide substrate is indicated in red.

Cr(III) oxide (21.5 mg.m^{-2}) and low (2.5 mg.m^{-2}) Cr(III) alternative substrates as well as ECCS, and the Cr(III) alternative produced via the one-step electrodeposition method are shown in Figs. 2a, b, c and d respectively.

The SEM images of the Cr(III) alternative substrates show that the steel substrate is heterogenous with evidence of varying rolling roughness. It was also observed that the Cr coating follows the structure of the substrate. Defects, approximately 1–2 µm in diameter, as highlighted by the red circles, were observed on the surface of both the two-step Cr(III) coated samples. Features above the surface appear lighter. Hence, the defects were identified as small, darker areas and explained as holes in the Cr coating allowing underlying iron to be exposed. However, the number of defects present was far greater for the sample with the lower Cr(III) oxide coating weight (2.5 mg.m^{-2}) as shown in Fig. 2b. Similarly, the steel substate of ECCS, Fig 3c, exhibited heterogeneities, like many industrial substrates, and the coating followed the structure of the

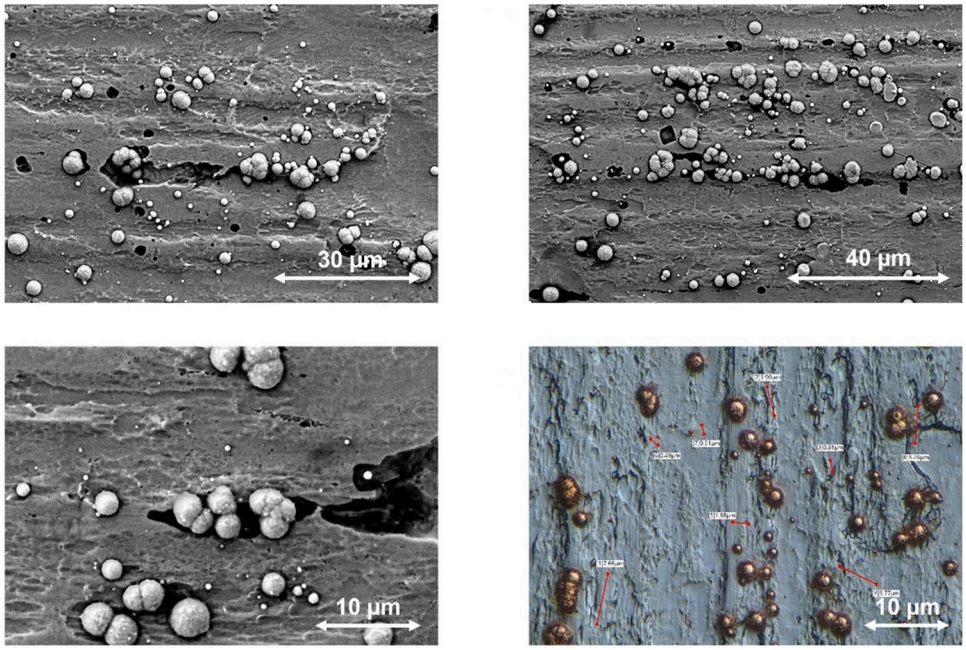

Fig. 3. SEM and optical imagery of the Cr(III) alternative substrate with a Cr(III) oxide coating weight of 3 mg.m^{-2} showing copper on its surface after a $CuSO_4$ dip.

substrate. However, the presence of defects on ECCS was minimal. Numerous defects were also present on Cr(III) alternative produced via the one-step electrodeposition method, Fig. 2d.

To quantify the number defects and how these varied between coating weights, a copper sulphate test was conducted. Samples of the Cr (III) alternative and ECCS were dipped in a copper sulphate solution, the composition of which can be found in Table 2 and left for 60 s before being rinsed under a stream of DI water and left to dry.

In this basic reaction, iron displaces copper ions from an aqueous solution of copper sulphate. It is a single displacement reaction of one metal by another metal which is realised through iron placing above copper in the reactivity series of materials; this therefore makes iron more reactive. Metallic iron is converted into ferrous ion (Fe^{2+}), and cupric ions (Cu^{2+}) are converted into metallic copper, *Eq. (1)*.

$$Fe(s) + Cu^{2+}(aq) \rightarrow Fe^{2+}(aq) + Cu(s) \quad (1)$$

Hence, at defects where iron is exposed, Cu will precipitate whilst the remainder of the intact substrate will be free of Cu. Due to this being a quick displacement reaction, and not copper plating, the copper formed is a precipitate and so is not formally adhered to the surface of the substrate. For this reason, it is important not to wipe the samples dry after the $CuSO_4$ dip, and instead let them drip dry as the deposited nodules are easily removed mechanically. SEM imagery of precipitated copper on substrates surfaces and optical imagery of these copper nodules and their relative sizes is shown in Fig. 3.

As seen in Fig. 3, the copper nodules have a characteristic 'mushroom' shape, being circular in most cases, with a significant height profile from the substrates surface. SEM imagery has shown that the shape of these defects is not consistent, so it is noted that this shape of copper precipitation is independent of the defect or iron it may precipitated in or on. To ensure that the nodules witnessed on the surface of these substrates were in fact copper, XRF measurements and EDX mapping were conducted. By varying the light settings and contrast on the Keyence optical microscope, it is possible to define these copper nodules more clearly, to use a colour contrast tool to calculate the area average of copper on a given sample. Using this method, the area of copper present on the surface, and hence an estimate of the area populated with defects was quantified using XRF. The results are shown in Fig. 4.

As shown in Fig. 4, increasing the Cr(III) oxide coating weight caused a decrease in the area ratio of copper, and hence, a decrease in the amount of defects present on the surface of the substrate. The Cr(III) alternative with a Cr(III) oxide coating weight of 3 $mg.m^{-2}$ had a copper area ratio of 5.6 %. This decreased to a copper area ratio of 2.2 % when the coating weight was increased to 23.5 $mg.m^{-2}$. ECCS exhibited the lowest copper area ratio of approximately 1.8 %, confirming that minimal defects, and thus exposed underlying iron, were present.

4.2. Electrochemical characterisation

All materials were characterised in terms of their OCP in 1 wt.% NaCl, pH 2 (acidified by the addition of HCl), solution typical of that found inside a filament head, due to the high concentration of chloride ions [3]. This would help determine whether the coating would anodically dissolve when coupled to the iron substrate. The OCP measurements enabled the corrosion potentials associated with varying Cr(III) alternative samples to be determined. The Cr(III) alternative samples were immersed in solution for 2 h where they were free to corrode. This allowed enough time for the OCP to stabilise (the potential was not significantly changing over time).

Table 2
Composition of copper sulphate solution used to visualise defects in chrome oxide layer on chrome oxide coated substrate materials.

Constituent	Weight / Volume
Copper Sulphate Pentahydrate	8 g
Sulphuric Acid	2 ml
DI Water	500 ml

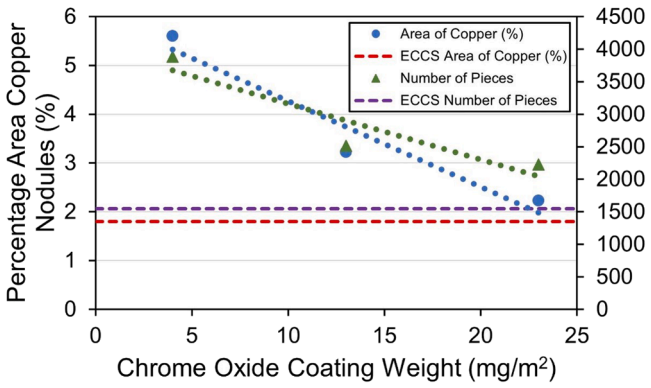

Fig. 4. Area ratio of copper on the surface of the Cr(III) alternative and ECCS substrate materials plotted with their respective site densities.

OCP measurements as a function of Cr(III) oxide coating weight are shown in Fig. 5 where the errors relate to ±one unit of standard deviation, on the basis of 2 consecutive measurements. The OCP measurements of blackplate and ECCS are also shown for comparison as the red and green point, respectively. The OCP measured for ECCS was more anodic relative to blackplate and the Cr(III) alternative. The OCP value for blackplate was similar to the samples of the Cr(III) alternative, thus suggesting that the exposed iron, as a result of defects in the coating, dominates the potential reading. Similarly, OCP values observed on the Cr(III) alternative electrodeposited via the one step method were also found to be similar to iron.

Potentiodynamic polarisation experiments were conducted with the intention to characterise the anodic and cathodic activity on varying Cr (III) oxide substrates, to help better understand the mechanism of FFC on these substrates. Cathodically, as shown in Fig. 6a, the samples with a relative high Cr(III) oxide coating weight were associated with 10 times lower current density. Thus, a trend was seen that linked higher oxide coating weights to lower cathodic currents. Anodically, there was less of a trend, and at a potential value of ~0 V vs. SHE (standard hydrogen

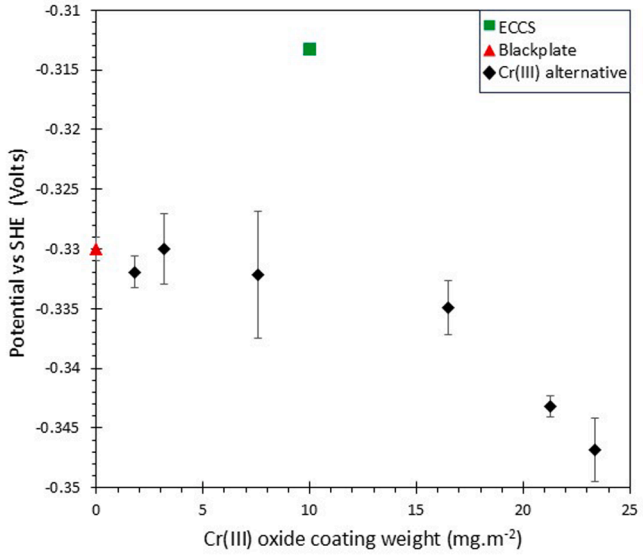

Fig. 5. Open circuit potential measurements as a function of Cr(III) oxide coating weight. The electrolyte used was 1 wt. % NaCl, pH 2. The red point represents iron, the green point ECCS and the black points represent varying Cr (III) oxide coating weights.

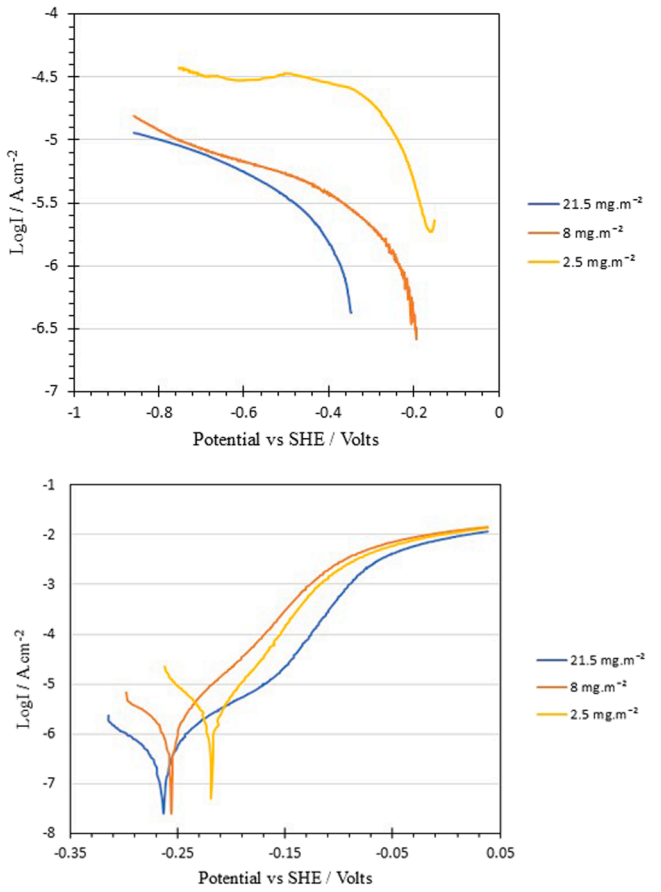

Fig. 6. Cathodic (a) and anodic (b) potentiodynamic polarisation curves for a relative low, medium and high Cr(III) oxide coating weight.

electrode) the current measured was the same for all substrates. The results are shown in Fig. 6b. This suggests that the measured current is primarily from the underlying iron substrate rather than the Cr(III) oxide layer.

4.3. Surface characterisation

XPS analysis, as shown in Fig. 7a–e, was used to determine and quantify the surface chemistry of the outermost layer (5 nm) of both a relative low and high Cr(III) oxide coating weight (2.5 and 21.5 mg.m^{-2} respectively) in the view that this outermost layer will dictate to what extent FFC propagates. This was performed on the as-received samples, prior to FFC initiation. ECCS, and the Cr(III) alternative produced via the one-step electrodeposition method, were also analysed for comparison purposes. Fig. 7a–e shows the XPS wide scans and chemical compositions of the outermost layer of these coatings. Fig. 7a shows that there were similarities between the surface scans for both the low and high coating weights and ECCS, with chromium peaks being present at 575 eV and 584 eV as well as the oxygen peak at 530 eV [17]. The iron peak was also present at 708 – 711 eV [27] but was larger for the lower Cr(III) oxide sample, suggesting more iron was present at the surface, most likely due to the reduced coating weight and presence of more defects. It is shown in the bar charts (Figs. 7b, c, d and e) that the chemical constituents of the outermost layer vary between the two Cr(III) oxide coating weights. Approximately 90x more $Cr(OH)_3$ was observed in the case of the sample with 21.5 mg.m^{-2} oxide compared with that of the sample with 2.5 mg.m^{-2}. Also, a significant quantity of iron was present on the surface of the 2.5 mg.m^{-2} sample in comparison to the 21.5 mg.m^{-2} sample. The chemical constituents of the outermost layer of ECCS comprise of a mixture of Cr_2O_3, Cr metal and $Cr(OH)_3$, with very little iron present. In contrast, the Cr(III) alternative produced via the one-step electrodeposition method had a large amount of Fe oxide present.

4.4. FFC experiments

A systematic study into the influence of Cr(III) oxide coating weight on the initiation and propagation of FFC was then completed. Fig. 8 shows samples of varying Cr(III) oxide coating weight (21.5 mg.m^{-2}, 13.5 mg.m^{-2}, 8 mg.m^{-2} and 3 mg.m^{-2} respectively), 4 weeks after FFC was initiated using 2 µl 0.05 M $FeCl_2$. Fig. 8 also shows images at weekly intervals of a sample with a relative low Cr(III) oxide coating weight. Visually, it appeared that the area of FFC significantly increased when the Cr(III) oxide coating weight was decreased. In turn, this may be linked to the increased porosity observed in the lower coating weights, as demonstrated by the copper sulphate tests. FFC initiated within the first week and continued to propagate during the following weeks. The filaments projected perpendicular to the scribe defect as is typically seen with this substrate [22]. Some of the filaments appeared to be made up of a series of 'dots' or blisters, and the filiform appeared to 'jump' to the next propagation site. These filaments also appeared to cross over one another. This was more noticeable in the samples with lower Cr(III) oxide coating weights. Filiform propagated in a similar manner to the lower Cr(III) oxide coating weights for the Cr(III) alternative electrodeposited via the one step method. The filaments were made up of interconnected pit like circular features. In contrast to the Cr(III) coatings described above, FFC did not occur on ECCS 4 weeks after initiation with $FeCl_2$. Also of note was the absence of red-brown iron rust in the scribe of the ECCS sample.

Fig. 9 shows an SEM image of a sample 4 weeks after FFC was initiated, where blisters in the coating were observed due to the propagation of FFC. At these blisters, cracks in the coating were seen along some of the filaments. These blisters in the Cr(III) coating were more prevalent on the samples with a relative lower Cr(III) oxide coating weight.

Computerised image analysis was performed to calculate the area of FFC present on each sample. Fig. 10 shows the total FFC corroded area, 4 weeks after FFC initiation, as a function of Cr(III) oxide coating weight. The error corresponds to ± one standard deviation on the mean of six measurements.

From Fig. 10, it is clear that the FFC corroded area was larger for samples with smaller Cr(III) oxide coating weight. The three samples with the lowest Cr(III) oxide coating weight (2.5 - 5.5 mg.m^{-2}) appeared to be significantly more susceptible to FFC than those with higher coating weights. These lower coating weights had an average FFC corroded area of 18.3 ± 2.7 mm^2. A Cr(III) oxide coating weight between 6.5 and 16.5 mg.m^{-2} significantly reduced the FFC corroded area to an average of 6.4 ± 1mm^2. The highest coating weights of 21.5 and 23.5 mg.m^{-2} exhibited the greatest resistance to FFC with an average FFC corroded area of 2.4 ± 0.05 mm^2. A comparatively low area of FFC was hence recorded at coating weights greater than 6.5 mg.m^{-2}, suggesting that a threshold value of approximately 6.5 mg.m^{-2} exists with regards to inhibiting FFC.

In comparison with the one-step process of producing the Cr(III) alternative, a Cr(III) oxide coating weight of 7 mg.m^{-2}, following 4 weeks of propagation, exhibited a FFC corroded area of approximately 14.5 mm^2; over 1.5 times that observed on a comparable sample made via the two-step deposition process. A coating weight of 24 mg.m^{-2} exhibited a FFC corroded area of 7.2 mm^2, approximately 3 times more than that observed on a comparable sample deposited via the two-step process. Thus highlighting the improvements that the two-step process offers with regards to inhibiting FFC.

Fig. 11 shows the FFC corroded area as a function of time for each of the Cr(III) oxide coating weights. The rate of FFC was relatively linear during the first two weeks of growth, but beyond this, the change in FFC corroded area was somewhat stifled and the rate of FFC appeared to

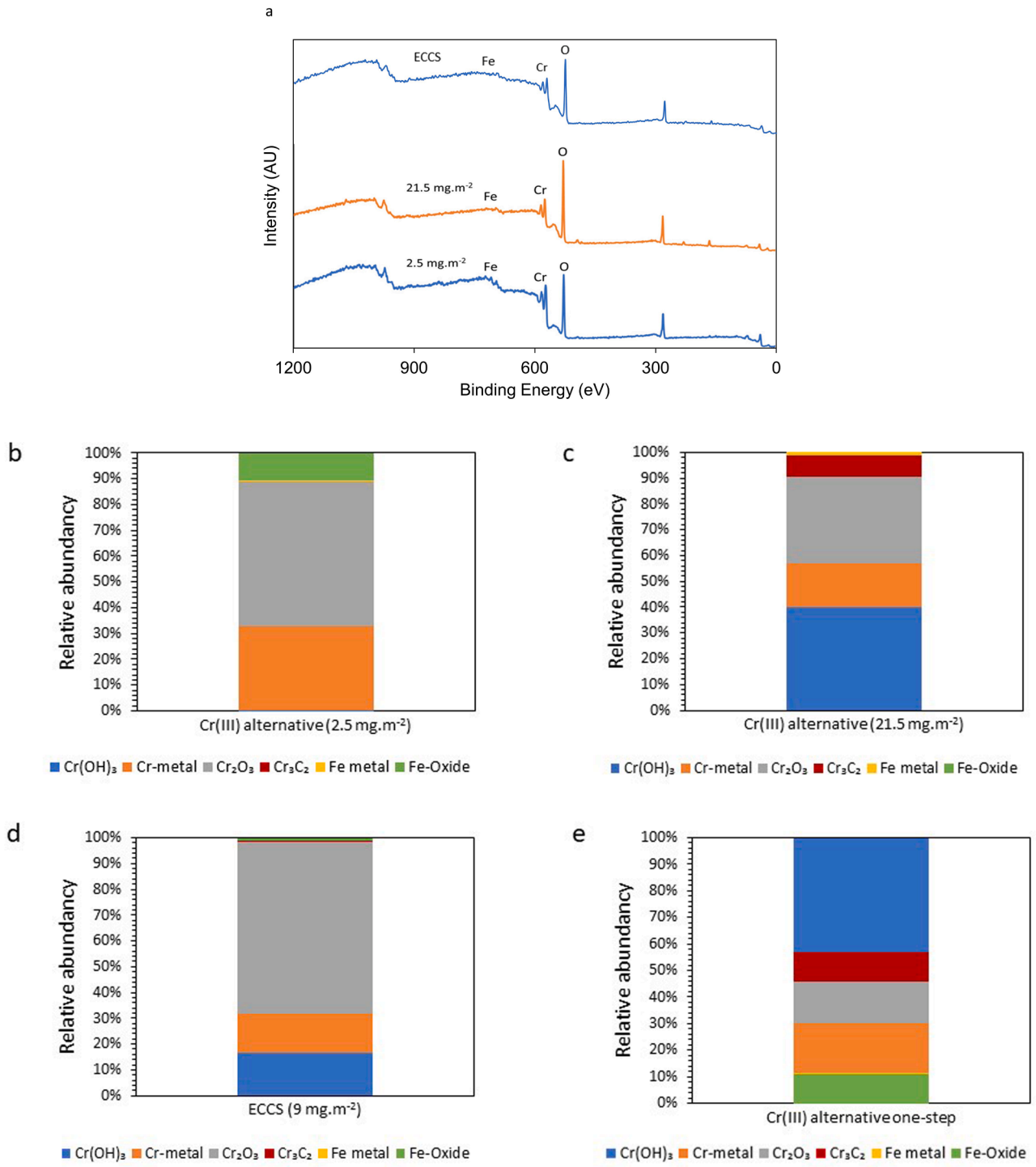

Fig. 7. XPS wide scans (a) and surface compositions (b) of as received ECCS and the Cr(III) alternative samples with a relative low and high Cr(III) oxide coating weight (2.5 and 21.5 mg.m^{-2} respectively). The surface composition of the Cr(III) alternative produced via the one step method is also shown for comparison purposes.

have reduced. The error bars correspond to ± one standard deviation on the mean of six measurements. It is of note that this decrease in rate of FFC was also observed on the samples produced via the one-step deposition process.

Table 3 shows the average corroded area for the different Cr(III) oxide coating weight samples as a function of time. The rate of FFC for the sample with the lowest Cr(III) oxide (2.5 mg.m^{-2}) decreased from an initial value of 16.5 mm^2 from week 0–2, to 3.4 mm^2 from week 2–4. On average, across the sample set, a 4.3 times reduction in FFC rate is observed between weeks 0–2 to weeks 2–4. A larger reduction in FFC rate between weeks 0–2 and 2–4 was observed for lower Cr(III) oxide coating weights. In Table 3, it can clearly be seen that the increase in FFC corroded area is inversely proportional to the thickness of Cr(III) oxide layer.

4.5. Post corrosion analysis

After FFC had been initiated with $FeCl_2$ and left to propagate for 4

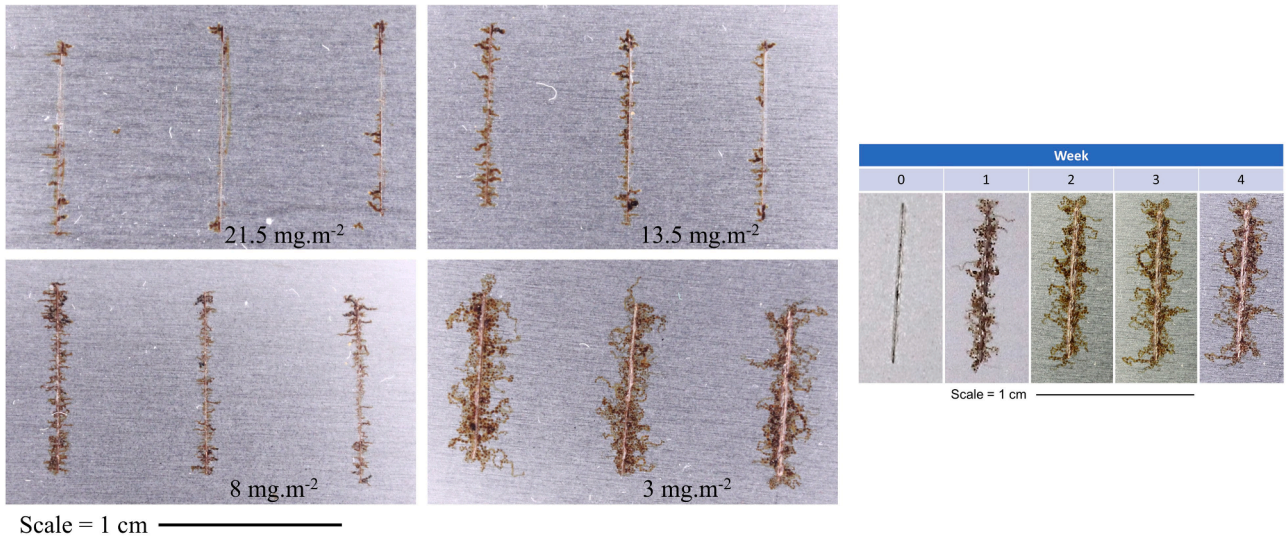

Fig. 8. The optical appearance of samples decreasing in Cr(III) oxide coating weight, 4 weeks after FFC was initiated with 2 μl of 0.005 M $FeCl_2$. The Cr(III) oxide coating weights were 21.5 mg.m^{-2}, 13.5 mg.m^{-2}, 8 mg.m^{-2} and 3 mg.m^{-2}, respectively. Images at weekly intervals after FFC was initiated from a scribe defect using $FeCl_2$, of the Cr(III) alternative sample with a relative low Cr(III) oxide coating weight is shown on the right of the figure.

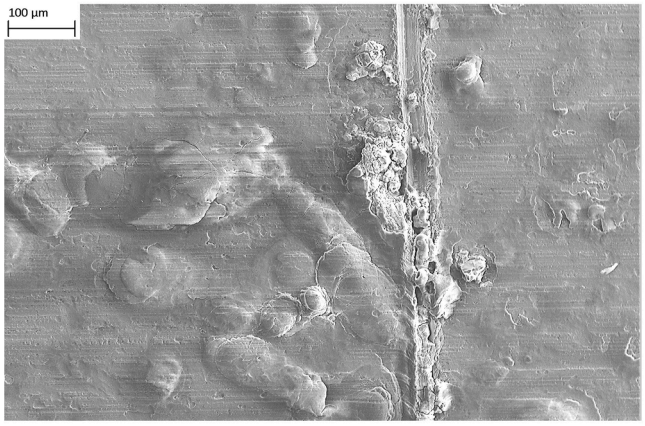

Fig. 9. SEM image of the surface of the Cr(III) alternative, 4 weeks after FFC was initiated with 2 μl of 0.005 M $FeCl_2$, where blisters in the coating were observed due to the propagation of FFC.

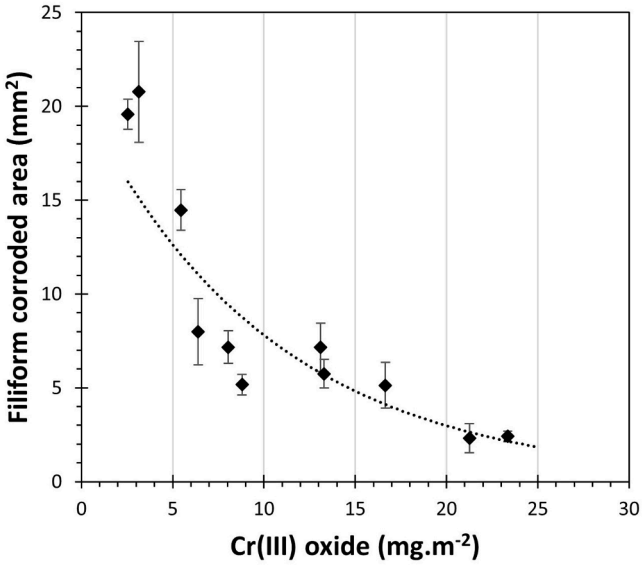

Fig. 10. FFC corroded area 4 weeks after initiation of FFC from a PVB scribe defect using 2 μl of 0.005 M $FeCl_2$ as a function of Cr(III) oxide coating weight.

weeks, optical microscope images were taken to look at the individual FFC filaments. The width of the filaments was observed to decrease with distance from the scribe defect, producing a tapered effect. Fig. 12 shows an example of the tapering filaments that were observed.

Measurements of the width of filaments at various distances from the filiform head were recorded using measuring tools on the microscope's software. Table 4 shows the average rate of change of the width of the filaments. The width of the filament is shown to decrease as it gets closer to the active head and thus, end of the filament, confirming the assumption that the filaments were tapering. Tapering of the filaments was more prominent on the samples with lower Cr(III) oxide coating weights.

Filament tapering has previously been associated with chloride entrapment, whereby chloride ions are left behind in the filament meaning less electrolyte is available for FFC to propagate [23]. There would thus be a change in the activity of the head electrolyte, and halting of the rate of FFC propagation. ToF-SIMS was used to determine the likelihood of this hypothesis.

ToF-SIMS was used to create a chemical image which provided a macro scale overview of the surface chemistry present on the samples. More specifically, it was used to analyse the chemical composition of the filaments and determine the distribution of certain elements including Cl^-. Fig. 13 shows a chemical image of one of the Cr(III) alternative samples where FFC had propagated. The scribe can be seen towards the bottom of the image with the filaments protruding perpendicular to the scribe (towards the top of the figure image). The pink colour denotes Cl^- and was present both at the front leading edge of the filament head, but also throughout the length of the filaments. Oxygen and hydroxides were also both present across a large proportion of the surface, indicative of corrosion product. The presence of Cl^- within the tail suggests it has become entrapped, meaning less electrolyte will be available for filiform propagation, and hence explains the tapering of filaments.

5. Discussion

The results demonstrate that, in comparison to ECCS, on which FFC was not observed, FFC was shown to initiate and propagate on the Cr(III) alternative, with the FFC corroded area being smaller at higher Cr(III)

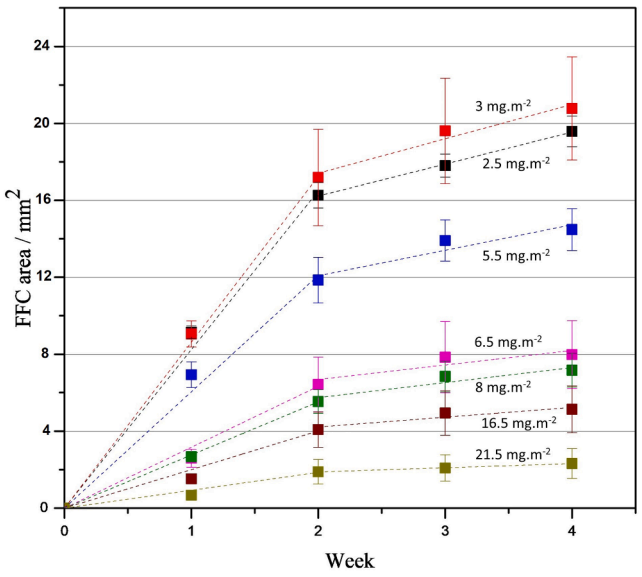

Fig. 11. Rate of FFC corroded area over 4 weeks as a function of Cr(III) oxide coating weight. The dotted lines represent the linear regression for weeks 0–2 and 2–4 individually.

Table 3
Average FFC corroded area on the Cr(III) alternative samples of varying Cr(III) oxide coating weight.

	FFC corroded area / mm^2						
Time / weeks	2mg. m^{-2}	3 mg. m^{-2}	5.5 mg. m^{-2}	6.5 mg. m^{-2}	8 mg. m^{-2}	16.5 mg. m^{-2}	21.5 mg. m^{-2}
0–2	16.5 ± 0.6	17.3 ± 0.2	12.1 ± 0.7	6.3 ± 0.3	5.5 ± 0.1	4.0 ± 0.3	1.8 ± 0.1
2–4	3.4 ± 0.1	3.2 ± 0.7	2.6 ± 0.8	1.5 ± 0.8	1.60 ± 0.6	1.0 ± 0.4	0.40 ± 0.02

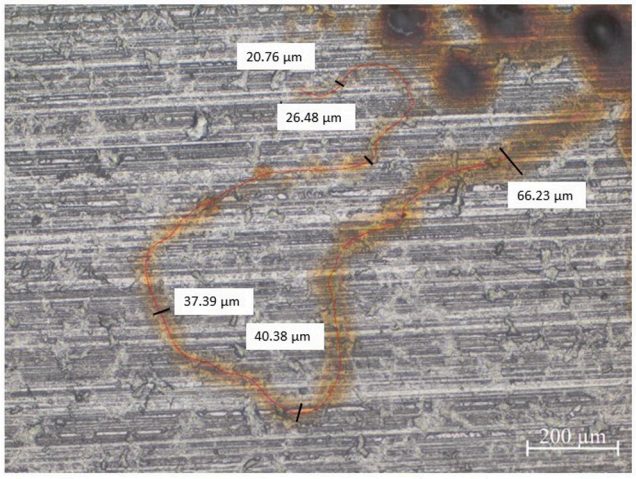

Fig. 12. An optical image of a FFC filament that is tapering on the surface of the Cr(III) alternative substrate. Measurements correspond to the width of the filament at different distances from the active head.

oxide coating weights. The FFC corroded area was significantly less for equivalent Cr(III) alternative samples produced via the two-step method, in comparison to the one-step process. The rate of FFC remained linear during the first 2 weeks of FFC propagation. After 2 weeks had passed, there was over a 4 times reduction in the rate of FFC propagation, and the rate of FFC plateaued.

Table 4
The average rate of change of the width of the FFC filaments.

Length from active head (µm)	*1600*	*1200*	*500*	*100*
Percentage loss in width of filament relative to starting point at 1600µm (%)	N/A	27 ±4.8	60 ±8.4	68 ±10.9

The difference in filiform corrosion resistance of the various Cr(III) coatings can be attributed to numerous factors. For instance, the SEM images of the Cr(III) alternative coatings, both one and two-step, show that the coatings are relatively imperfect with the presence of numerous penetrative defects relative to the surface of ECCS. During the production of ECCS, the electroplating process involves the rapid reduction of Cr (VI) to Cr onto iron, which is relatively noble. Thus, little iron is exposed through the coating. In comparison, the electrodeposition of Cr (III) based coatings is caused by a local upwards shift in pH at the steel (cathode) surface [16]. This pH shift is driven by the evolution of H_2 at the steel strip, which may block deposition of Cr and lead to the formation of defects, such as pores in the Cr electrodeposit. Furthermore, the number of defects was greater for samples with lower Cr(III) oxide coating weights as shown by SEM and copper sulphate testing. The samples with lower Cr(III) oxide coating weights had numerous filaments made up of blisters. We propose that these filaments were advancing via a successive pitting-mechanism whereby the majority of the surface was unaffected by corrosion, but individual pits were observed between these uncorroded areas. The formation of these pits can be observed in Video 1.

It is thought that these filaments were able to advance forward by 'jumping' to the next available defect or area of exposed iron in the coating. This mechanism has been proposed previously in work by Edy [28]. It is envisaged that after corrosion has been initiated at the artificial scribe in the coating, some of these propagate further, lifting the coating in doing so. This allows the corrosive environment to progress under the coating. It is proposed that at defects and areas of weakness in the coating, corrosion pits are formed that penetrate the Cr coating. This penetrative pressure, will again lift the coating, allowing the propagation of the filament. Hence, due to the increased amount of defects, as well as the thinner nature of the coatings with lower Cr(III) oxide coating weights, the filaments would be able to propagate more easily.

It is proposed that the presence of these defects was the cause of the OCP values being similar to those of iron. The presence of iron on the surface of the Cr(III) alternative substrates, confirmed by XPS data would cause an increase in anodic processes, and may explain the more negative OCP values in comparison to ECCS (Fig. 7). These defected areas would be more susceptible to anodic dissolution than the chromium layer itself.

Given that FFC propagation is driven by the coupling of anodic and cathodic reactions via an electrolyte, inhibition of either reaction will slow the overall corrosion process. Equally, changes in electrolyte composition, such as the sequestering of anions like chloride into an oxide film, could further slow FFC propagation.

Due to the alkaline conditions at the back of the FFC head, the favoured cathodic reaction should be the oxygen reduction reaction (ORR). ORR can occur via a $2e^-$ or $4e^-$ process, or a combination of the two. In the case of iron, the possible 2 electron reactions are:

$$O_2 + 2e^- + 2H_2O \rightarrow 2OH^- + H_2O_2$$

$$HO_2^- + H_2O + 2e^- \rightarrow 3OH^-$$

The possible 4 electron reaction is:

$$O_2 + 2H_2O + 4e^- \rightarrow 4OH^-$$

It has previously been shown [19] that on Cr(III) alternative substrates ORR occurs via a 2 electron process, whilst on iron it predominantly follows the 4 electron route. This means that the ORR occurs on

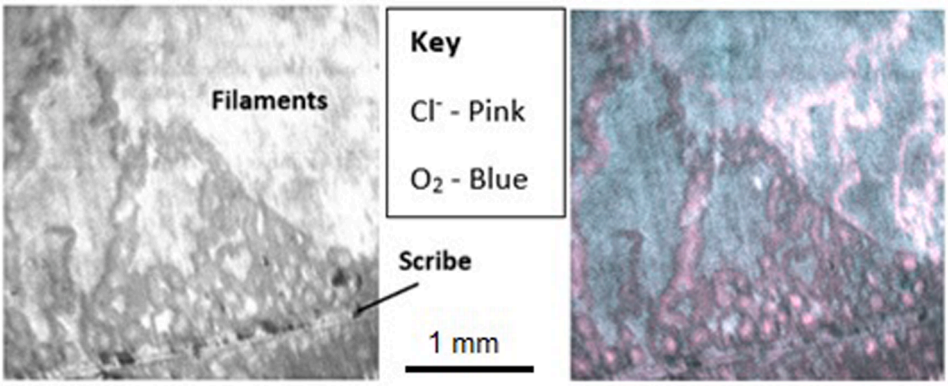

Fig. 13. ToF-SIMS chemical image of the elemental surface composition of the Cr(III) alternative specimen subjected to FFC. The pink colour is representative of Cl^- and the blue colour O_2.

Cr(III) alternative substrates with half the current than that seen on iron. In turn, this demonstrates how Cr/Cr(III)oxide coatings act as a poor cathode for ORR in comparison to iron and explains why the corrosion rate is lower on for higher Cr(III) coating weights.

The reduction in cathodic activity implies that the Cr(III) oxide layer may be limiting electron transfer to oxygen reduction sites. This suggests that, at higher thicknesses electron transfer will be further limited, in turn disrupting the cathodic reaction required for FFC growth. This is consistent with the cathodic polarisation data, whereby the lower Cr(III) oxide coatings exhibited greater cathodic currents. Since FFC progresses by maintaining an active cathode-anode separation, disrupting cathodic activity weakens the corrosion filament's ability to advance.

Moreover, the increased FFC corroded area observed for lower Cr(III) oxide coating weights suggests that Cr(III) oxide is serves as a barrier to FFC. Beyond its role as a physical barrier that reduces permeability to corrosive species, Cr_2O_3, offers insulating characteristics due to its semiconductor properties; it has a wide band gap of around 3 eV indicating more energy is required to excite an electron compared with most transition metal-oxides [29]. Electron transfer is associated with the cathodic oxygen reduction reaction towards the back of the FFC filament head as seen in Fig. 1. Again, this correlates to the lower cathodic currents observed for higher Cr(III) oxide coating weights. Moreover, it has been shown previously [19] that Cr(III) coatings with elevated levels of Cr(III) oxide were more resistant to corrosion-driven cathodic delamination. It was shown that the ohmic behaviour of the Cr(III) oxide was consistent with its known wide band-gap semiconductor properties, and that interfacial electron transfer would be impaired on such oxide covered electrode surfaces. It is therefore plausible that Cr(III) oxide may play a similar role in resisting interfacial electron transfer between the anode and cathode at the front and back of the filament head respectively. Indeed, this would be consistent with the diminished rates of FFC propagation observed here for Cr(III) coatings with elevated levels of Cr(III) oxide.

Another possibility is that FFC propagation rates on the Cr(III) coatings are surface controlled (by processes occurring at the electrolyte-substrate interface such as electron transfer) or controlled by mass transport in the electrolyte. Previous studies by Williams et al. have shown that when FFC propagation rates are surface controlled (i.e. electron transfer limited), the rate is strongly dependent on the quantity of electrolyte in the head. In such cases, the rate is shown to be proportional to the interfacial area present between the filament-head electrolyte droplet and the metal substrate. This is in resemblance to the results found in this study, where the substrates with a greater Cr(III) oxide coating weight, and thus larger interfacial area, exhibited a lower rate of FFC.

However, a significant finding of the FFC results is the decreased propagation rate of FFC over the 4-week time period. There could be several explanations for the reduction of rate observed in the current study. Initially, two potential mechanisms were proposed. Firstly, being, that the cathode may form in the defect, where iron, an active oxygen cathode is exposed [30]. If this were the case the distance between anode and cathode, over which they couple, would increase as the filament length increased over time. This would cause a greater ohmic resistance of the electrolyte and would result in a reduction in corrosion rate. Secondly, it is possible that the tapering occurs as a result of the change in head electrolyte composition.

In considering all the observations in the current study, the propagation of underfilm FFC on Cr(III) coatings is similar to that on organic coated iron, whereby anodic attack of the Cr(III) coating at the filament leading edge is followed by a filament tail consisting of corrosion product. However, one difference observed for organic coated Cr coatings studied here, is the tapering of the filament tail during the process of FFC propagation. Although the conservation of chloride ions within the filament head, resulting from migration to the anodic leading edge to maintain electroneutrality, is observed, a proportion of chloride is also removed through entrapment in the corrosion product contained in the filament tail.

The primary anodic reaction is as follows:

$$Fe \rightarrow Fe^{2+} + 2e^-$$

The reaction between Fe^{2+} and OH^- at the cathodic site can lead to the formation of insoluble iron hydroxides (e.g., $Fe(OH)_2$ and $Fe(OH)_3$). This can deplete Fe^{2+} from solution, indirectly influencing chloride ion movement by reducing the driving force for its migration. Localised alkalisation at the filament tail due to OH^- accumulation may also promote the precipitation of certain iron-chloride compounds, potentially affecting chloride availability at different points along the filament. Given that uncoated steel/iron exhibits linear kinetics, and parabolic kinetics were observed on this Cr(III) coated steel, it suggests that the Cr coating is indeed playing a crucial role in the entrapment of chloride ions. It is proposed that chloride ions also form complexes with Cr(III), leading to the formation of a chloride-containing passive film, explained in a process elsewhere [31].

Thus, as the chloride ion concentration within the filament head electrolyte reduces, the underfilm corrosion cell becomes less capable of maintaining filament propagation and may explain the tapering phenomenon observed. Indeed Kousis et al. [32] observed a similar phenomenon on organically coated magnesium alloys, whereby a high abundance of chloride was found not only at the leading edge of the filament, but also along the filament's entire length. In turn, this also led to a reduction in FFC propagation rate because of the depletion in chloride ions from the filament head electrolyte due to their entrapment within corrosion product deposits in the tail. Cristoforetti et al. [33] also observed aggressive contaminant ions including Cl^- along the filament

on acrylic-coated steel.

In summary, this work establishes that variations in the Cr(III) oxide coating weight can have significant impacts on the susceptibility of the Cr(III) alternative to FFC. Most notably, increasing the Cr(III) oxide coating weight improves the ability of the Cr(III) alternative to withstand FFC. It is proposed that a higher Cr(III) oxide coating weight provides improved insulating properties and better surface coverage, ultimately protecting the underlying substrate.

6. Conclusion

Cr(III) oxide was shown to provide some resistance with regards to inhibiting the extent of FFC, and an improvement in FFC resistance was seen compared to samples produced via the one-step deposition process. The results suggest that the samples with lower Cr(III) oxide coating weights are more susceptible to FFC than the higher oxide coating weights. This is proposed to occur for two reasons. Firstly, 1) lower oxide coatings are shown to contain a greater number of defects, thus allowing for the ingress of electrolyte to the substrate beneath. This would cause the coating to be broken down at a more rapid rate due to ingress of the electrolyte through the micropores in the coating to substrate iron and/or Secondly, 2) the insulating properties that Cr(III) oxide offers would allow samples with greater coating weights to block the electron transfer reaction even more, thus slowing the rate of the cathodic reaction.

It was also found that the linear growth rate of FFC decreased with time. This is proposed to be a result of chloride entrapment in the tail of the filament such that the volume of chloride ions in the head reduced with time. As the conservation of chloride ions is required for continued FFC propagation, the implication is a reduced rate of FFC, ultimately leading to the termination of FFC propagation.

The present work displayed how FFC was initiated and propagated on the novel, bilayer Cr(III) alternative, composed of two distinct layers, in comparison to the current standard, ECCS. An industrially scaled Cr (III) alternative would need to surpass a Cr(III) oxide coating weight of 6.5 $mg.m^{-2}$ (whilst the Cr layer remains at 100$mg.m^{-2}$) to have a FFC corroded area <8 mm^{-2} over a 4-week time period. If the Cr(III) oxide coating weight is too low, this work suggests that it would not provide sufficient corrosion protection compared to ECCS.

CRediT authorship contribution statement

E. Bluett: Writing – review & editing, Writing – original draft, Visualization, Methodology, Investigation, Formal analysis, Data curation, Conceptualization. **J. Edy:** Supervision, Data curation, Writing – review & editing, Writing – original draft. **M. Dodd:** Data curation, Writing – original draft. **A.C.A. de Vooys:** Supervision. **N. Wint:** Visualization, Validation, Supervision, Conceptualization, Writing – original draft. **E. Jewell:** Supervision. **H.N. McMurray:** Supervision.

Declaration of competing interest

The authors declare that they have no known competing financial interests or personal relationships that could have appeared to influence the work reported in this paper.

Data availability statement

All data supporting this study are provided in full in the 'Results' section of this paper.

Acknowledgements

The authors would like to thank the Materials and Manufacturing Academy (M2A), Swansea University, funded from the European Social Fund via the Welsh Government (c80816), the Engineering and Physical Sciences Research Council via the COATED 2 Centre for Doctoral Training (CDT, Grant Ref: EP/L015099/1), the Welsh European Funding Office (WEFO) and Tata Steel UK Ltd that has made this research possible. The authors would also like to thank Dr Christian Mescall, Tata Steel, Research and Development, and Dr Tom Dunlop, Advanced Imaging of Materials (AIM), Swansea University, for their help with this project.

Supplementary materials

Supplementary material associated with this article can be found, in the online version, at doi:10.1016/j.electacta.2025.145943.

References

[1] Tata Steel, "Tata-steel-packaging-tinplate-product-range-EN. 2005 ".
[2] B. Boelen, H.Den Hartog, and H. Van Der Weijde, "Product performance of polymer coated packaging steel, study of the mechanism of defect growth in cans," vol. 50, pp. 40–46, 2004, doi:10.1016/j.porgcoat.2003.09.011.
[3] H.N. Mcmurray, G. Williams, and E.B. Emeraldine, "Under film /coating corrosion $," no. July 2015, pp. 1–19, 2016, doi:10.1016/B978-0-12-803581-8.01601-5.
[4] C.F. SHARMAN, Filiform underfilm corrosion of lacquered steel surfaces, Nature 153 (May 1944) 621.
[5] A. Cristoforetti, S. Rossi, F. Deflorian, M. Fedel, Recent Progress in Understanding Filiform Corrosion On Organic Coated steel: A comprehensive Review, Elsevier B. V., Jul. 01, 2024, https://doi.org/10.1016/j.porgcoat.2024.108469.
[6] R.B. Figueira, R. Sousa, C.J.R. Silva, Multifunctional and smart organic–inorganic hybrid sol–gel coatings for corrosion protection applications. Advances in Smart Coatings and Thin Films For Future Industrial and Biomedical Engineering Applications, Jan. 2020, pp. 57–97, https://doi.org/10.1016/B978-0-12-849870-5.00008-2.
[7] M.G.S. Ferreira, M.L. Zheludkevich, J. Tedim, Advanced protective coatings for aeronautical applications. Nanocoatings and Ultra-Thin Films, 2011, pp. 235–279, https://doi.org/10.1533/9780857094902.2.235.
[8] C. Hahin, R.G. Buchheit, Filiform corrosion. Corrosion: Fundamentals, Testing, and Protection, Dec. 2003, pp. 248–256, https://doi.org/10.31399/ASM.HB.V13A.A0003614.
[9] G.M. Hoch, A review of filiform corrosion, in: Localised Corrosion, 134, NACE, Houstan, 1974.
[10] A. Cristoforetti, J. Izquierdo, R.M. Souto, F. Deflorian, M. Fedel, S. Rossi, In-situ measurement of electrochemical activity related to filiform corrosion in organic coated steel by scanning vibrating electrode technique and scanning micropotentiometry, Corros. Sci. 227 (Feb. 2024), https://doi.org/10.1016/j.corsci.2023.111669.
[11] O. Øystein, A.F. Knudsen, *Corrosion Control Through Organic Coatings*, Second, Taylor & Francis, New York, 2017.
[12] Y. Deng, M. Wang, T. Tian, S. Lin, P. Xu, and L. Zhou, "The effect of hexavalent chromium on the incidence and mortality of Human cancers : a meta-analysis based on published epidemiological," vol. 9, no. February 2019, doi:10.3389/fonc.2019.00024.
[13] T. Petry, R. Knowles, and R. Meads, "An analysis of the proposed REACH regulation," vol. 44, no. 2006, pp. 24–32, 2007, doi:10.1016/j.yrtph.2005.07.007.
[14] L. Li, A.L. Desouzac, G.M. Swain, In situ pH measurement during the formation of conversion coatings on an aluminum alloy (AA2024), The Royal Society of Chemistry (2013).
[15] A. Cristoforetti, S. Rossi, F. Deflorian, M. Fedel, Exploring the role of passivating conversion coatings in enhancing the durability of organic-coated steel against filiform corrosion using an electrochemical simulated approach, Prog. Org. Coat. 189 (Apr. 2024), https://doi.org/10.1016/j.porgcoat.2024.108357.
[16] J.H.O.J. Wijenberg, "Method for manufacturing chromium-chromium oxide coated substrates," US 2016/0138178 A1, 2016.
[17] J.H.O.J. Wijenberg, M. Steegh, M.P. Aarnts, K.R. Lammers, J.M.C. Mol, Electrodeposition of mixed chromium metal-carbide-oxide coatings from a trivalent chromium-formate electrolyte without a buffering agent, Electrochim. Acta 173 (2015) 819–826, https://doi.org/10.1016/j.electacta.2015.05.121.
[18] N. Wint, A.C.A. de Vooys, H.N. McMurray, The corrosion of chromium based coatings for packaging steel, Electrochim. Acta 203 (2016) 326–336, https://doi.org/10.1016/j.electacta.2016.01.100.
[19] J.E. Edy, H.N. McMurray, K.R. Lammers, A.C.A. deVooys, Kinetics of corrosion-driven cathodic disbondment on organic coated trivalent chromium metal-oxide-carbide coatings on steel, Corros. Sci. 157 (Aug. 2019) 51–61, https://doi.org/10.1016/j.corsci.2019.04.037.
[20] J. Wijenberg, M. Steegh, J.P. Penning, and I.Portegies Zwart, "Wo 2014/079909," 2014.
[21] J.H.O.J. Wijenberg, A.J. Wittebrood, and M.W. Litz, "Method for manufacturing chromium-chromium oxide coated blackplate," WO2019121582A1, 2019.
[22] G. Williams, C. Kousis, N. McMurray, P. Keil, A mechanistic investigation of corrosion-driven organic coating failure on magnesium and its alloys, Npj. Mater. Degrad. 3 (1) (2019), https://doi.org/10.1038/s41529-019-0103-4.
[23] G. Williams, H.N. Mcmurray, E.S. Lett, G. Williams, and H.N. Mcmurray, "Anion-exchange inhibition of filiform corrosion on organic coated AA2024-T3 aluminum alloy by hydrotalcite-like pigments Anion-exchange inhibition of filiform corrosion

on organic coated AA2024-T3 aluminum alloy by hydrotalcite-like pigments," pp. 9–12, 2003, doi:10.1149/1.1539771.
[24] J. Campbell, Properties of castings. Complete Casting Handbook, Jan. 2015, pp. 447–528, https://doi.org/10.1016/B978-0-444-63509-9.00009-1.
[25] G. Williams, H.N. McMurray, The mechanism of group (I) chloride initiated filiformcorrosion on iron, Electrochem. commun. 5 (2003) 871–877.
[26] "Introduction to mass analyzers: SHIMADZU (Shimadzu Corporation)." Accessed: Jul. 22, 2022. [Online]. Available: https://www.shimadzu.com/an/service-support/technical-support/analysis-basics/fundamental/mass_analyzers.html.
[27] J.-C. Wang, et al., Synergistic photocatalysis of Cr(VI) reduction and 4-chlorophenol degradation over hydroxylated α-Fe2O3 under visible light irradiation, J. Hazard. Mater. 311 (Jul. 2016) 11–19, https://doi.org/10.1016/j.jhazmat.2016.02.055.
[28] J.Edward Edy, "Corrosion of organic coated trivalent chromium coated technology steel (TCCT)".
[29] M.M. Abdullah, F.M. Rajab, and S.M. Al-abbas, "Structural and optical characterization of Cr 2 O 3 nanostructures : evaluation of its dielectric properties," vol. 027121, pp. 1–11, 2014, doi:10.1063/1.4867012.
[30] N. Wint, S. Geary, H.N. Mcmurray, G. Williams, A.C.A. De Vooys, The kinetics and mechanism of atmospheric corrosion occurring on tin and iron-tin intermetallic coated steels The kinetics and mechanism of atmospheric corrosion occurring on tin and iron-tin intermetallic coated steels, Electrochem. Soc. 162 (2015), https://doi.org/10.1149/2.0681514jes.
[31] L. Bjornkvist and I. Olefjord, "The electrochemistry of chromium in acidic chloride solutions: anodic dissolution and passivation," 1991.
[32] C. Kousis, P. Keil, H.N. McMurray, G. Williams, The kinetics and mechanism of filiform corrosion affecting organic coated Mg alloy surfaces, Corros. Sci. 206 (Sep. 2022), https://doi.org/10.1016/j.corsci.2022.110477.
[33] A. Cristoforetti, F. Deflorian, S. Rossi, M. Fedel, On the occurrence of filiform corrosion on organic-coated carbon steel exposed to cyclic aging test, Corrosion 79 (12) (Dec. 2023) 1339–1344, https://doi.org/10.5006/4443.